ISPRS Journal of Photogrammetry and Remote Sensing 212 (2024) 1–12

Contents lists available at ScienceDirect

ISPRS Journal of Photogrammetry and Remote Sensing

journal homepage: www.elsevier.com/locate/isprsjprs

Towards real-time processing for UAV-mounted GPR-SAR imaging systems

María García-Fernández [a,*], Guillermo Álvarez-Narciandi [a], Jaime Laviada [b], Yuri Álvarez López [b], Fernando Las-Heras [b]

[a] Centre for Wireless Innovation, Queen's University Belfast, Northern Ireland Science Park, Queen's Road, Queen's Island, Belfast, BT3 9DT, United Kingdom
[b] Área de Teoría de la Señal y Comunicaciones, Universidad de Oviedo, Campus Universitario de Gijón, 33203, Gijón (Asturias), Spain

ARTICLE INFO

Keywords:
Unmanned Aerial Vehicles
Ground Penetrating Radar
Synthetic Aperture Radar
Landmines
Improvised Explosive Devices
Phase Shift Migration

ABSTRACT

Ground Penetrating Radar (GPR) systems mounted on Unmanned Aerial Vehicles (UAVs) are becoming a promising solution to inspect beneath the soil surface. In particular, resorting to Synthetic Aperture Radar (SAR) techniques, these systems are able to retrieve subsurface radar images, in which buried targets can be detected. However, one of the major bottlenecks of this technology is the significant amount of time required for computing the radar images (due to the usage of computationally expensive algorithms to handle non-regular acquisition domains). To face this challenge, this work proposes an efficient interpolation approach, combining a height shift operation with a 2D interpolation, that enables the adoption of a migration algorithm called Phase Shift Migration (PSM). As a result, the processing time is drastically improved, offering close to real-time operation. The proposed methodology has been validated in a realistic scenario for detecting buried explosive targets, comparing it with conventional backprojection techniques in terms of image quality and processing time.

1. Introduction

The integration of Ground Penetrating Radar (GPR) systems on board Unmanned Aerial Vehicles (UAVs) has experienced significant growth in the last few years (Alvarez Lopez et al., 2022; Catapano et al., 2022). This trend has been favored by the progress of UAV technology, and the advantages arising from UAV-mounted GPR systems (which enable the inspection of remote areas without being in contact with the soil). Furthermore, GPR systems are able to detect both metallic and dielectric buried targets (provided there is enough dielectric contrast between the target and the surrounding soil). As a result, UAV-mounted GPR systems are suitable for a wide range of applications (Garcia-Fernandez et al., 2020; Jenssen et al., 2020; Wu et al., 2019; Grathwohl et al., 2021) in numerous fields (such as security and defense, non-destructive testing and environmental monitoring).

A particular area in which UAV-mounted GPR systems are becoming a promising alternative is in the detection of landmines and Improvised Explosive Devices (IEDs), as these systems eliminate the risk of accidental detonation during the inspection (Garcia-Fernandez et al., 2018; Sipos and Gleich, 2020). In most cases, the objective is to retrieve a high-resolution radar image of the subsurface in which the targets can be detected. For this purpose, the radar measurements are coherently combined, relying on the Synthetic Aperture Radar (SAR) paradigm, which in turn requires a high positioning accuracy.

UAV-mounted GPR-SAR systems have been already tested for detecting buried targets (Burr et al., 2021), even in realistic scenarios (García-Fernández et al., 2022). In addition, different techniques have been developed to improve their focusing capabilities and/or the detection performance. As an example, in García-Fernández et al. (2022) a clutter reduction technique based on Singular Value Decomposition (SVD) has been proposed, and in Grathwohl et al. (2023) a modification of the backprojection (SAR) algorithm is developed to account for a tilted ground surface. More recently, a novel architecture (using an array of antennas) has been proposed to increase the scanning throughput (i.e., the area inspected per time) (García-Fernández et al., 2023).

Most UAV-mounted GPR-SAR systems employ a backprojection algorithm (such as Delay And Sum, DAS Johansson and Mast, 1994) to retrieve the radar images of the subsurface, as this kind of SAR algorithm can work with measurements gathered at arbitrary positions (i.e., they do not need to lie on a regular grid) (Garcia-Fernandez et al., 2020). This is particularly important when dealing with UAV-mounted systems, as it is not possible to acquire measurements following an ideal regular/uniform grid. In addition, backprojection algorithms can be tailored to different radar architectures (including fully multistatic

* Corresponding author at: Centre for Wireless Innovation, Queen's University Belfast, Northern Ireland Science Park, Queen's Road, Queen's Island, Belfast, BT3 9DT, United Kingdom.
E-mail address: m.garcia-fernandez@qub.ac.uk (M. García-Fernández).

https://doi.org/10.1016/j.isprsjprs.2024.04.008
Received 1 January 2024; Received in revised form 11 March 2024; Accepted 12 April 2024
Available online 27 April 2024

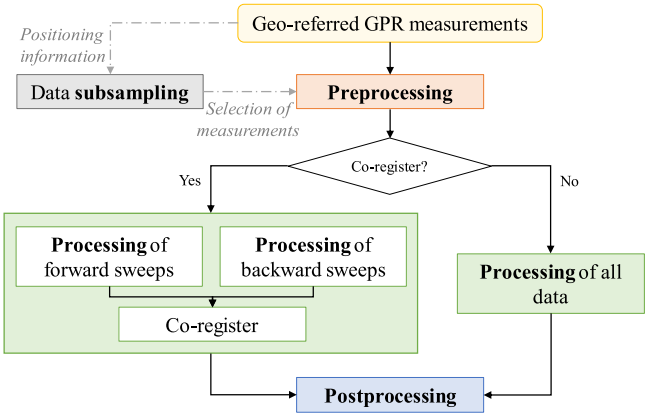

Fig. 1. Flowchart of the GPR-SAR imaging processing chain. (For interpretation of the references to color in this figure legend, the reader is referred to the web version of this article.)

geometries García-Fernández et al., 2021, 2023) and the investigation domain (i.e., the area or volume in which the radar image is retrieved) can be defined independently from the observation domain (i.e., the domain that comprises the measurement positions). However, the main drawback of backprojection algorithms is their computational complexity.

Another class of algorithms suitable for processing measurements gathered with a UAV-mounted GPR is microwave tomography (Noviello et al., 2021; Catapano et al., 2022). These algorithms, which are based on solving a linearized inverse scattering problem, can also handle arbitrarily distributed measurements, and can provide imaging results with improved resolution (compared to backprojection algorithms) (Gennarelli et al., 2023) at the expense of further increasing the computational complexity.

In fact, one of the major bottlenecks of UAV-mounted GPR systems is the time required for processing the measurements to retrieve the radar image of the subsoil, as they currently rely mostly on backprojection algorithms. A common approach to perform GPR imaging relies on migration algorithms (such as Stolt migration Stolt, 1978), which are usually based on performing Fast Fourier Transform operations. As a result, they are computationally efficient, but they require that the measurements lie in a uniform, planar grid. Therefore, they cannot be applied to UAV-based GPR systems (Catapano et al., 2022; Noviello et al., 2022; Gennarelli et al., 2023) as the flight paths yield significantly non-regular acquisitions (Grathwohl et al., 2023).

For free-space applications with irregular acquisition domains, such as free-hand imaging (Narciandi et al., 2021), the usage of migration algorithms has been studied by resorting to the projection of multistatic multi-planar data onto a virtual planar array (Vasileiou et al., 2022) or by relying on compressive sensing approaches to estimate missing samples (Regmi et al., 2021). However, the adoption of migration techniques for UAV-mounted GPR measurements remains unexplored.

This article proposes a method which, combining a height shift operation to project the measurements on a single horizontal plane with an efficient 2D interpolation, enables for the first time the adoption of migration algorithms in UAV-mounted GPR systems to retrieve 3D GPR-SAR images. Results from experimental flights show that the proposed approach enables not only a drastic reduction in the processing time compared to backprojection and tomography-based approaches, but also yields an improvement in the quality of the retrieved images. The effectiveness of the proposed strategy has been validated in the context of buried explosive targets detection, achieving an improvement in the processing time of more than three orders of magnitude with respect to the conventional backprojection approach.

The article is organized as follows. Section 2 provides an overview of the UAV-mounted GPR-SAR system employed in this contribution, including the system architecture and the signal processing chain. The proposed methodology to achieve close to real-time processing is explained in Section 3. Section 4 includes the experimental validation using GPR measurements gathered during flight tests. Finally, the conclusions are drawn in Section 5.

2. System description

This section provides an overview of the UAV-mounted GPR-SAR system employed in this work, both in terms of hardware and radar signal processing.

2.1. Architecture

The UAV-mounted GPR-SAR prototype used in this work has been presented in Garcia-Fernandez et al. (2018, 2019, 2020) and García-Fernández et al. (2022). In addition to the usual subsystems on board conventional UAVs (flight controller, positioning sensors and communication devices), a radar subsystem and a high accuracy positioning subsystem have been integrated to enable GPR-SAR applications.

The radar subsystem comprises an ultra-wide-band radar and three Vivaldi antennas. The radar can operate from 100 MHz up to 6 GHz, with one transmitting port and two receiving ports working simultaneously. The antennas frequency band ranges from 600 MHz to 6 GHz. However, due to the lower penetration into the soil of high frequencies, only the frequency band within 600 MHz to 3 GHz is considered for GPR-SAR processing.

The conventional positioning sensors on board the UAV include an inertial measurement unit (IMU) to provide attitude information (comprising an accelerometer, a gyroscope and a magnetometer); a barometer that gives an estimation about the height; and a Global Navigation Satellite System (GNSS) receiver that provides position and velocity information. However, in order to coherently combine the radar measurements (i.e., to enable SAR processing), the positions where measurements are acquired must be known with high accuracy (i.e., with an error much smaller than the minimum operating wavelength). For this purpose, a multi-band multi-constellation Real Time Kinematic (RTK) receiver has been mounted on board the UAV. This device provides an accuracy around 0.5 cm in the horizontal plane and 1 cm in the vertical direction. In addition, a laser rangefinder is also integrated into the UAV to provide an estimation of the height over the soil surface. This height estimation is used by the UAV to keep a predefined steady height from the soil surface during the inspection.

The working principle of the UAV-mounted GPR-SAR system consists of autonomously flying over the area under inspection following a predefined rectangular measurement grid. The radar measurements are continuously gathered during the flight and sent to a ground-control station in real-time (together with the synchronized positioning information).

2.2. GPR-SAR imaging

The geo-referred radar measurements acquired with the UAV are processed according to the flowchart depicted in Fig. 1 (Garcia-Fernandez et al., 2019) and García-Fernández et al. (2022).

Although the UAV predefined flight path is a rectangular grid, internal and external disturbances (such as wind gusts) cause that the actual UAV flight path deviates from the predefined one. This, together with changes in the UAV speed along the flight, results in a non-uniform acquisition domain which, besides, is non-planar. For this reason, a data subsampling technique is established to select the measurements that will be processed. As explained in Garcia-Fernandez et al. (2022), its goal is to discard those measurements which could worsen the resulting GPR-SAR image (e.g., avoiding over-sampled areas).

The preprocessing comprises several clutter mitigation techniques (average subtraction and distance-based singular-value-decomposition filtering García-Fernández et al., 2022) as well as the estimation of the UAV height from the radar measurements (as explained in García-Fernández et al. (2022)).

The core step in the flowchart shown in Fig. 1 is the processing of the measurements, i.e., their coherent combination. This processing, which provides a radar image of the inspected scenario, has been usually performed using the DAS algorithm (Johansson and Mast, 1994) or a variation called masked SAR (Garcia-Fernandez et al., 2020). These algorithms are based on coherently adding the preprocessed radar measurements weighted by a phase correction term. As previously explained, they have been used for processing UAV-mounted radar measurements due to their ability to work with arbitrarily distributed data, at the expense of a high computational complexity. In this contribution, the usage of the Phase Shift Migration (PSM) algorithm to process UAV-mounted GPR measurements is proposed to efficiently retrieve the 3D GPR-SAR image. As it will be explained in Section 3, the main advantage of this algorithm is its reduced execution time (thanks to the use of Fourier-based operations). However, it requires the measurements to be uniformly acquired in a planar domain and, thus, it cannot be directly applied to measurements gathered with a UAV-mounted GPR prototype. For this reason, an efficient interpolation approach has been developed.

Regardless of the algorithm used to combine the GPR measurements, the processing chain can also include a technique called co-registration. Its goal is to compensate for slightly different tilt angles of the GPR antennas with respect to the ground during forward and backward sweeps. This issue, explained in García-Fernández et al. (2022), can cause a small defocusing in the resulting GPR-SAR images. In case of applying co-registration, the forward and backward sweeps are processed independently, and the resulting GPR-SAR images are co-registered based on their intensity (García-Fernández et al., 2022).

Finally, the resulting GPR-SAR image can be postprocessed to extract some further information. For instance, a Constant False Alarm Rate (CFAR) detector can be applied to automatically detect potential buried targets (García Fernández et al., 2021).

3. Methodology

This section presents the methods that enable the use of migration techniques with non-regular acquisition domains in the context of UAV-mounted GPR scenarios, as well as the migration algorithm employed to retrieve the subsurface radar images.

3.1. Efficient interpolation of the measurements

As aforementioned, the proposed approach to efficiently interpolate the GPR measurements combines a height shift operation (to project them on a single horizontal plane) together with a 2D interpolation (based on Delaunay triangulation). It should be noted that these methods are independent of the particular hardware or measurement platform, provided the radar measurements are geo-referred with enough accuracy. In the following subsections, without loss of generality, the radar measurements are assumed to be time-domain (or, equivalently, range-domain) signals.

3.1.1. Height shift

The first step to efficiently interpolate the radar measurements consists of shifting them in range. The goal of this step is to mimic that all the measurements are gathered at the same $z-$coordinate, so that later only a 2D interpolation is required.

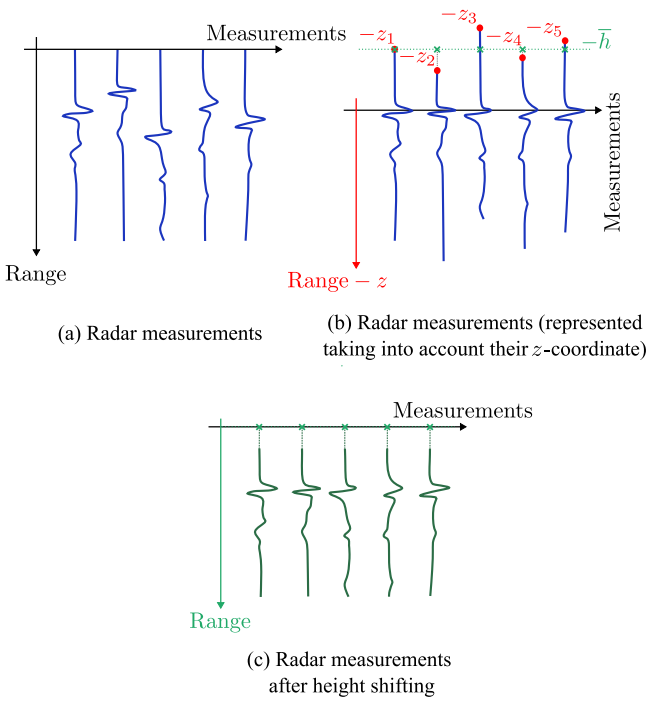

Fig. 2. Scheme illustrating the height shift operation.

This height shift operation is illustrated in Fig. 2, where it can be observed that the measurements are shifted as if they were all gathered at the same $z-$coordinate (in particular, at $z = \overline{h}$, where $\overline{h}$ is the mean UAV height). After this shift, the measurements are also trimmed so that all of them have the same length.

In particular, Fig. 2(a) depicts a set of raw radar measurements represented as a function of range. In Fig. 2(b) the same set of radar measurements is depicted but in this case taking into account the $z-$coordinate where each radar measurement was gathered. For instance, the first measurement starts at $-z_1$, which means that the UAV was flying at a height of z_1 (over the soil surface, which is assumed to be at $z = 0\,\text{m}$) when this measurement was acquired. Finally, Fig. 2(c) shows that, after the height shift operation is performed, the transformed radar measurements mimic that they were all gathered at the same $z-$coordinate. It should be noted that this operation is performed within the preprocessing of the radar measurements (orange box in Fig. 1).

It is also of interest to analyze the accuracy of this height shift operation. The total distance traveled by a wave from $\boldsymbol{r}_m$ (the measurement position) to $\boldsymbol{r}'$ (the target's position) is given by: $R_{\text{T}} = R_{\text{air}} + \sqrt{\varepsilon_r} R_{\text{soil}}$, where R_{air} denotes the distance traveled in air (from $\boldsymbol{r}_m$ to $\boldsymbol{r}_i$, being $\boldsymbol{r}_i$ the refraction point at the air–soil interface), ε_r is the soil permittivity and R_{soil} denotes the distance traveled within the soil (from $\boldsymbol{r}_i$ to $\boldsymbol{r}'$). According to the scheme shown in Fig. 3 and the Snell's law, these distances can be computed by solving (1) to estimate the refraction point ($\boldsymbol{r}_i$), taking into account that this point lies also in the plane of incidence.

$$\frac{\sqrt{R_{\text{air}}^2 - h^2}}{R_{\text{air}}} = \sqrt{\varepsilon_r} \frac{\sqrt{R_{\text{soil}}^2 - d^2}}{R_{\text{soil}}} \tag{1}$$

In case of normal incidence (i.e., $D = 0\,\text{m}$) and when the radar measurement is taken at $z = h$, the reflection from a target buried at $z = -d$ is detected at $R_{\text{T}}(z = h) = h + \sqrt{\varepsilon_r} d$. If, instead, the measurement is taken at $z = h + \Delta h$, the target is detected at $R_{\text{T}}(z = h + \Delta h) = (h + \Delta h) + \sqrt{\varepsilon_r} d$. Therefore, shifting this measurement by a value of Δh

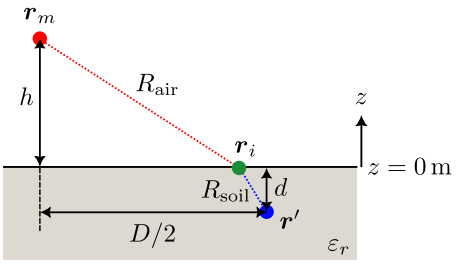

Fig. 3. Scheme illustrating the computation of R_T.

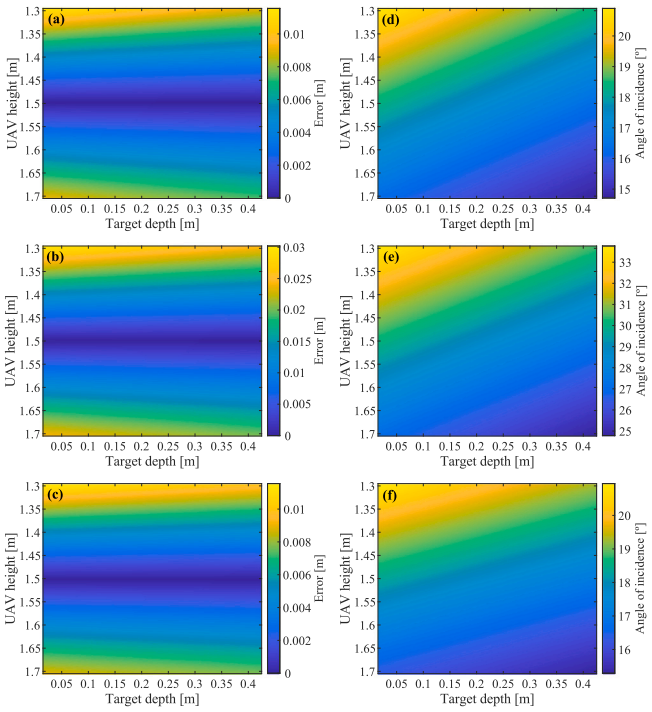

Fig. 4. Error in the range induced by the height shift (left column) and angle of incidence (right column) as a function of UAV height and target depth for: $D = 1\,\text{m}$, $\varepsilon_r = 4$ (a, d), $D = 1.75\,\text{m}$, $\varepsilon_r = 4$ (b, e), and $D = 1\,\text{m}$, $\varepsilon_r = 10$ (c, f).

does not induce any error as $R_{\text{T}}(z = h + \Delta h) - \Delta h = R_{\text{T}}(z = h)$. However, for oblique incidence (i.e., $D \neq 0$), the height shift operation induces a small error in the range at which the target is detected because $R_{\text{T}}(z = h + \Delta h) - \Delta h \neq R_{\text{T}}(z = h)$.

The error produced when approximating $R_{\text{T}}(\overline{h} + \Delta h)$ by $R_{\text{T}}(\overline{h}) + \Delta h$ is given by: Error $= |R_{\text{T}}(\overline{h} + \Delta h) - (R_{\text{T}}(\overline{h}) + \Delta h)|$. This error has been analyzed for variations of the UAV height in the interval $\overline{h} \pm 0.20\,\text{m}$ (i.e., $[1.3, 1.7]\,\text{m}$ as $\overline{h} = 1.5\,\text{m}$) and for target depths between $0.02\,\text{m}$ and $0.42\,\text{m}$. In addition, different values of soil permittivity (ε_r), and horizontal distance between the measurement point and the target ($D/2$) have been considered. It should be noted that the latter is upper bounded as the incident angle in the soil cannot be greater than the critical angle. The critical angle, given by (2), corresponds to the incident angle for which the refracted angle is 90°.

$$\theta_c = \sin^{-1}\left(\frac{1}{\sqrt{\varepsilon_r}}\right) \tag{2}$$

Fig. 4 shows the error in the range estimation (left column) and the angle of incidence (right column) for different values of D and ε_r. In all cases, it can be observed that, for the same target depth, the error increases as the UAV height differs from $\overline{h} = 1.5\,\text{m}$ (i.e., as $|\Delta h|$ increases), and the error is larger for $\overline{h} - |\Delta h|$ than for $\overline{h} + |\Delta h|$. For the same UAV height, the error decreases with the target depth. Comparing the first case ($D = 1\,\text{m}$ and $\varepsilon_r = 4$) with the second one ($D = 1.75\,\text{m}$ and $\varepsilon_r = 4$), it can be concluded that the error increases with the distance between the measurement position and the target (i.e., with $D/2$). Finally, comparing the first and third case ($D = 1\,\text{m}$ and $\varepsilon_r = 10$), the error barely changes. The only exception to all these observations would occur when the angle of incidence is greater than the critical angle as the error is assumed to be zero since there would not be any backscattered wave from the target.

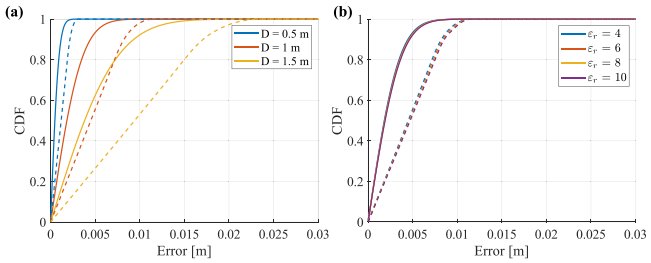

Fig. 5. CDF of the error in the range induced by the height shift for: $\varepsilon_r = 4$ and different values of D (a), and for $D = 1\,\text{m}$ and different values of ε_r (b). Solid line corresponds to a UAV height distribution following a Gaussian distribution and dash line results from considering a uniform distribution.

In order to further analyze this error, its cumulative density function (CDF) has been obtained for different values of D and ε_r (see Fig. 5). As in the previous analysis, the target depth uniformly ranges from $0.02\,\text{m}$ to $0.42\,\text{m}$. The UAV height distribution has been modeled following a uniform distribution (i.e., assuming the height varies uniformly between $1.3\,\text{m}$ and $1.7\,\text{m}$), and following a Gaussian distribution (with mean $\overline{h} = 1.5\,\text{m}$ and standard deviation $\sigma_h = 0.06\,\text{m}$), which better reflects the behavior of UAV height during flights. The CDFs obtained when considering the former (uniform) distribution are depicted with dash lines, whereas those obtained with the latter (Gaussian) distribution are plotted with solid lines. In agreement with the conclusions extracted from Fig. 4, the error increases with D and barely changes with ε_r (unless the angle of incidence exceeds the critical angle). It is worth mentioning that in all cases the error is well below the minimum working wavelength ($\lambda_{min} = 10\,\text{cm}$). In particular, when considering the realistic modeling of the UAV height and $D = 1\,\text{m}$, the error is always below $1\,\text{cm}$.

3.1.2. Interpolation in the horizontal plane

Due to the non-uniform movement of the UAV, the measurement positions do not lie on a regular grid and do not follow any order. It should also be noted that for each measurement position, the radar measurement contains $N_{r_{points}}$ points (as it is a time-domain or range-domain signal). After the height shift operation, the vertical or range coordinate follows a regular grid. Therefore, instead of performing a 3D interpolation, a 2D interpolation can be applied. To perform this interpolation efficiently, an interpolation surface is built as follows.

First, a Delaunay triangulation of the horizontal measurement positions (i.e., $x-$ and $y-$coordinates) is performed. The vertices of the triangles obtained with the Delaunay triangulation correspond to the measurement positions and, thanks to the height shift operation conducted in the previous step, all these triangles are in the same z plane. The interpolated $x-$ and $y-$ coordinates, which follow a regular grid, are also defined and, then, an interpolant surface is built triangle by triangle. Assuming a linear interpolation method, for each triangle the interpolant surface matches the data corresponding to each vertex. For a given point within the interpolated grid, called $\boldsymbol{P}_{int} = (x_{int}, y_{int})$, the triangle (of the Delaunay triangulation) which contains $\boldsymbol{P}_{int}$ is found. The associated vertices of this triangle (noted as $\boldsymbol{P}_1$, $\boldsymbol{P}_2$ and $\boldsymbol{P}_3$) are retrieved, and the barycentric coordinates of $\boldsymbol{P}_{int}$ (called $\boldsymbol{C}_{int} = (c_{1,int}, c_{2,int}, c_{3,int})$) are computed. The interpolated radar measurement at

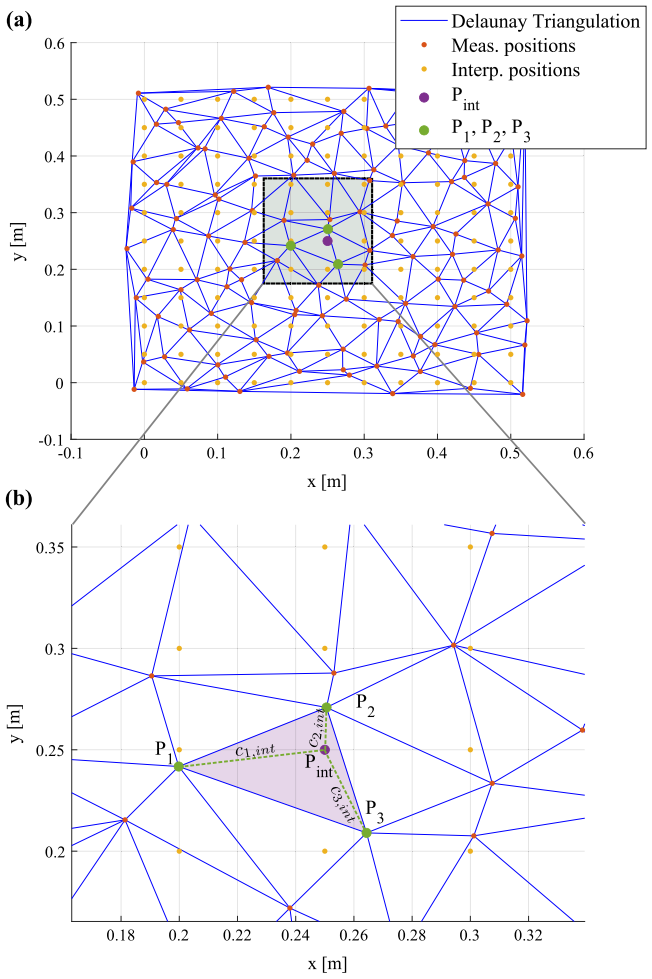

Fig. 6. Scheme illustrating the construction of the interpolant surface. (For interpretation of the references to color in this figure legend, the reader is referred to the web version of this article.)

this point $\boldsymbol{P}_{int}$, called $\boldsymbol{E}_{int}(\boldsymbol{P}_{int})$, is then computed as follows (Amidror, 2002):

$$\boldsymbol{E}_{int}(\boldsymbol{P}_{int}) = \boldsymbol{C}_{int} \cdot \begin{pmatrix} \boldsymbol{E}_{\boldsymbol{p}}(\boldsymbol{P}_1) \\ \boldsymbol{E}_{\boldsymbol{p}}(\boldsymbol{P}_2) \\ \boldsymbol{E}_{\boldsymbol{p}}(\boldsymbol{P}_3) \end{pmatrix}, \tag{3}$$

where $\boldsymbol{E}_{\boldsymbol{p}}(\boldsymbol{P}_1)$, $\boldsymbol{E}_{\boldsymbol{p}}(\boldsymbol{P}_2)$ and $\boldsymbol{E}_{\boldsymbol{p}}(\boldsymbol{P}_3)$ denote the radar measurements (after applying the preprocessing techniques) at points $\boldsymbol{P}_1$, $\boldsymbol{P}_2$ and $\boldsymbol{P}_3$. This operation is performed for all points within the interpolated grid and it is considered to be part of the processing step (depicted in green in Fig. 1).

The process of building the interpolant surface is illustrated in Fig. 6. In Fig. 6(a) the Delaunay Triangulation computed for a set of simulated measurement positions is plotted with a solid blue line, together with the measurement positions (in orange dots) and the interpolated positions (in yellow). In Fig. 6(b), the barycentric coordinates for a given point in the interpolated grid ($\boldsymbol{P}_{int}$) are depicted.

To illustrate the efficiency of this interpolation procedure, the improvement compared to performing a 3D interpolation is analyzed in Table 1 for a different number of measurement positions (N_{pos}) and points per measurement (i.e., $N_{r_{points}}$). This improvement is computed as the ratio between the time required for the 3D interpolation and the time needed with the proposed 2D approach (which takes advantage of the fact that the range coordinate is the same for all measurements after applying the height shift operation). It should be noted that this study has been performed by simulating the measurement positions and, for each configuration, the interpolation has been repeated 10 times to estimate the average interpolation time. The interpolation methods have been executed on a laptop equipped with a i7-8750H CPU.

Table 1
Comparison of the interpolation time when performing a full 3D interpolation and the proposed 2D approach.

N_{pos}	$N_{r_{points}}$	3D interp. [s]	2D interp. [s]	Improvement
10 201	400	180.56	0.1184	1525
10 201	200	87.95	0.0875	1005
5041	400	94.11	0.0723	1302
5041	200	43.79	0.0396	1106
2601	400	45.66	0.0300	1522
2601	200	22.57	0.0215	1050

The comparison shown in Table 1 clearly shows that the proposed approach is more than three orders of magnitude faster than a 3D interpolation, thus facilitating the real-time interpolation of the measurements.

3.2. Phase Shift Migration (PSM)

PSM is a processing method derived from the scalar wave equation and, as mentioned before, it requires the measurements to be acquired in a uniform planar grid (Fallahpour et al., 2014; González-Díaz et al., 2020). The uniform acquisition enables the usage of Fast Fourier Transform (FFTs) techniques to perform the Fourier Transform operation in a fast manner.

After performing the interpolation, a set of N_{int} interpolated radar measurements of $N_{r_{points}}$ points each is obtained. These interpolated measurements are denoted, for the sake of simplicity, as $\tilde{E}(x, y, t)$, where x, y are the interpolated horizontal coordinates, and t is the time-domain axis (as the radar works in the time-domain). As explained in the previous subsection, due to the height shift operation, the height of all measurements is considered to be $z = \overline{h}$. The first step in the PSM algorithm consists of performing a Fourier transform in the spatial and time domain coordinates (i.e., x, y and t), obtaining:

$$\tilde{E}(k_x, k_y, f) = \mathcal{F}_{xyt}\{\tilde{E}(x, y, t)\}, \tag{4}$$

where k_x and k_y are the wavenumber components in the $x-$ and y-axis, and f is the frequency. The symbol $\mathcal{F}$ denotes the Fourier transform and the subindexes denote the domains in which this operation is performed.

The reflectivity at a plane z', $\rho(z')$, is then given by:

$$\rho(z') \propto \mathcal{F}_{xy}^{-1}\left\{\sum_{n=1}^{N_f} \tilde{E}(k_x, k_y, f_n) e^{j\varphi_p(z')}\right\}, \tag{5}$$

where $\mathcal{F}^{-1}$ is the inverse Fourier transform and the frequency axis is assumed to be sampled at N_f points (i.e., $f \equiv \{f_n\}$, with $n = 1, \ldots, N_f$). The phase-shift $\varphi_p(z')$ is in turn computed as follows:

$$\varphi_p(z') = \begin{cases} k_{z_{0,p}}(\overline{h} - z'), & z' \geq 0 \\ k_{z_{0,p}}\overline{h} - k_{z_{s,p}} z', & z' < 0, \end{cases} \tag{6}$$

with $k_{z_{0,p}}$ and $k_{z_{s,p}}$ being the $z-$components of the wavenumber at the pth frequency in free-space and in the soil, respectively. These values can be computed as indicated in (7), where $k_{\text{medium},p}$ denotes the wavenumber in the medium (free-space or the soil) at the pth frequency.

$$k_{z_{\text{medium},p}} = \sqrt{4k^2_{\text{medium},p} - k_x^2 - k_y^2} \tag{7}$$

Recovering the reflectivity in a 3D imaging domain (i.e., retrieving a 3D radar image) just requires performing the operation stated in (5) for all the z' planes within the imaging domain.

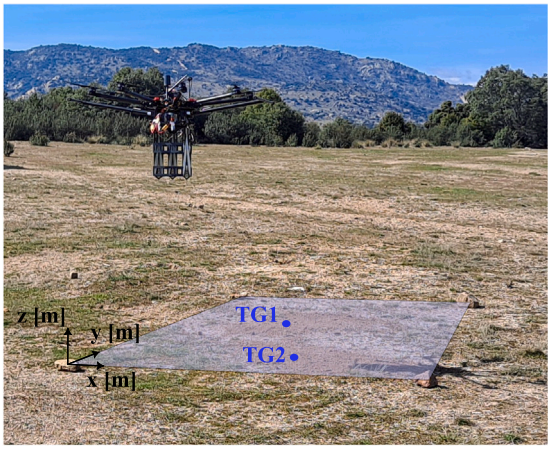

Fig. 7. Scenario of the initial flying tests. The inspected area is delimited by a blue rectangle and the position of the targets is indicated with blue dots. (For interpretation of the references to color in this figure legend, the reader is referred to the web version of this article.)

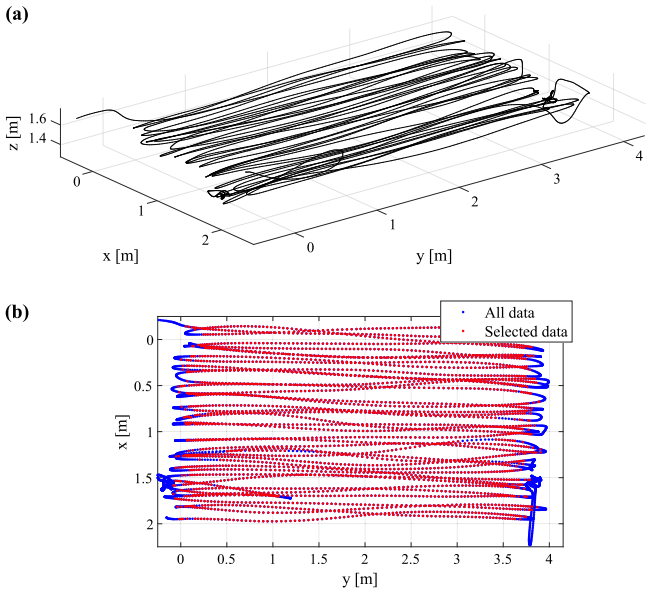

Fig. 8. Flight path (a) and measurement positions (b) in the initial tests (all positions in blue, and selected ones to be processed in red). (For interpretation of the references to color in this figure legend, the reader is referred to the web version of this article.)

It should be noted that if the permittivity of the soil is not taken into account (i.e., a homogeneous free-space scenario is assumed), the phase-shift φ_p is directly given by the first line of (6) for all values of z'.

4. Results

The proposed methodology has been validated with measurements gathered with the UAV-mounted GPR system presented in Section 2. Both the masked SAR backprojection algorithm (used in previous works Garcia-Fernandez et al., 2020) and the proposed approach have been compared, in terms of computational time and image quality (qualitatively and quantitatively). For masked SAR, the integration length (i.e., the mask size) has been set to $D_x = D_y = 2$ m (as integration lengths over this value do not yield valuable information).

Two different scenarios have been considered, a small scenario for the initial tests (presented in Section 4.1) and a realistic scenario with buried landmines and IEDs (Section 4.2). These validation scenarios are located at a Spanish military training and shooting range, located north of Madrid.

In both cases, the GPR measurements were acquired at a mean UAV height of $\overline{h} = 1.5$ m, as a trade-off between safety, flight stability, attenuation losses, and resolution. The inspected areas have been surveyed with the UAV autonomously following a rectangular grid, in which the along-track sweeps were separated $\lambda_{min}/2 = 0.05$ m, at a flight speed of 75 cm/s.

The permittivity of the soil has been estimated as $\varepsilon_r = 4$ (Alvarez et al., 2017) and it has been taken into account to retrieve the GPR-SAR images with the different processing algorithms.

4.1. Initial tests

The initial tests have been performed in an area of 2 m × 4 m, where two metallic flat disks have been buried at 13 cm depth. The diameter of the disks is around 20 cm for the first one (denoted as TG 1) and 15 cm for the second one (denoted as TG 2). A picture of the scenario during the inspection is shown in Fig. 7.

The flight path followed by the UAV is depicted in Fig. 8, where all measurement positions are shown in blue, and the selected positions to be processed are depicted in red. The number of selected positions is 3741 and, as aforementioned, at each measurement position, the two radar channels are measured simultaneously (which means that the total number of considered measurements is 7482). It should also be noted that in this scenario the autonomous flight was interrupted twice to emulate harder non-uniform conditions in order to test the subsampling strategies (as explained in Garcia-Fernandez et al. (2022)).

The interpolated coordinates correspond to a regular grid of 2 m × 4 m sampled at a uniform interval. Two different sampling intervals have been tested: $\lambda_{min}/4 = 0.025$ m and $\lambda_{min}/2 = 0.05$ m. The former results in 13 041 interpolated positions, whereas the latter yields 3321 interpolated positions.

The 3D GPR-SAR images are obtained in a volume of 2 m × 4 m × 0.4 m, discretized in voxels of $\Delta_{xy} \times \Delta_{xy} \times 0.01$ m (where Δ_{xy} is the discretization considered in the horizontal plane). This results in $41 \times 81 \times 41 = 136161$ voxels when $\Delta_{xy} = 0.05$ m and in $81 \times 161 \times 41 = 534681$ voxels if $\Delta_{xy} = 0.025$ m. As previously mentioned, backprojection algorithms allow to use any type of discretization, whereas in the case of PSM the discretization of the image is the same as the sampling of the (interpolated) measurement positions.

The backprojection algorithm (masked SAR) has been tested using both the original measurements and the interpolated data (following the proposed interpolation approach) in order to assess the effect of the interpolation in the results. Furthermore, both masked SAR and PSM have been compared with and without co-registration.

4.1.1. Qualitative radar image comparison

To compare the imaging results obtained with the different algorithms and parameters, two sections of the 3D GPR-SAR image corresponding to the top view of each target (at $z = -0.13$ m) have been selected. The reconstructions are shown in Fig. 9 for the first target and in Fig. 10 for the second one, considering the different processing algorithms.

When the radar image is discretized with a step of $\Delta_{xy} = \lambda_{min}/2 = 0.05$ m and co-registration is applied (first row of Figs. 9 and 10), both targets can be clearly distinguished, with the processing based on PSM providing images with less clutter. A higher clutter level is especially observed when masked SAR is applied using the original measurements. However, if the interpolation is performed before applying masked SAR, the clutter level is also reduced. Therefore, the proposed interpolation approach not only enables to use the PSM algorithm, but also contributes to reducing the clutter level.

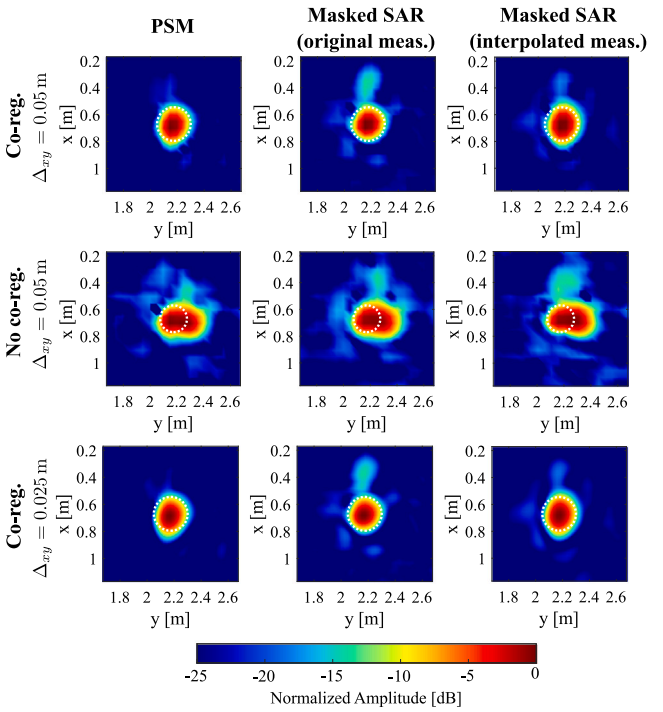

Fig. 9. Comparison of the radar images for the first target (at $z = -0.13$ m) when considering the different processing algorithms (PSM in the first column, masked SAR with the original data in the second column and masked SAR with the interpolated data in the third column). The discretization of the radar image is $\Delta_{xy} = 0.05$ m in the first two rows, and $\Delta_{xy} = 0.025$ m in the third one. Co-registration is considered in the first and third rows.

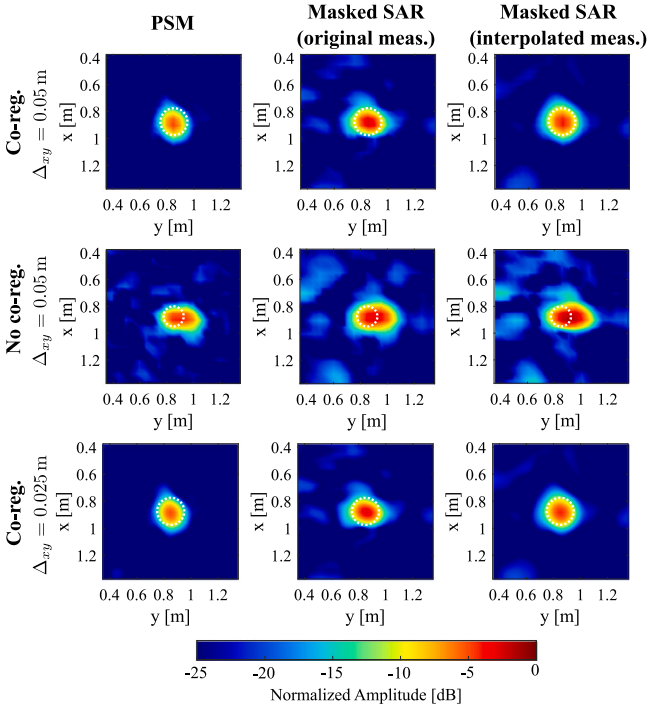

Fig. 10. Comparison of the radar images for the second target (at $z = -0.13$ m) when considering the different processing algorithms (PSM in the first column, masked SAR with the original data in the second column and masked SAR with the interpolated data in the third column). The discretization of the radar image is $\Delta_{xy} = 0.05$ m in the first two rows, and $\Delta_{xy} = 0.025$ m in the third one. Co-registration is considered in first and third rows.

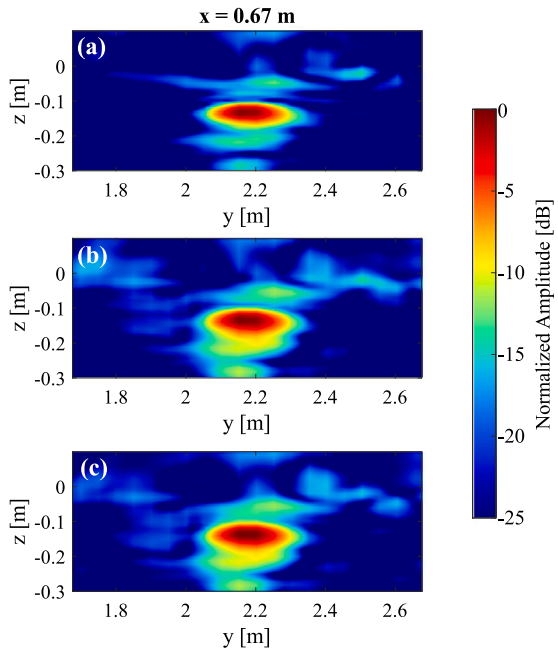

Fig. 11. Comparison of the radar images for the first target in a vertical cut (at $x = 0.67$ m) when considering the different processing algorithms: PSM (a), masked SAR with the original data (b) and masked SAR with the interpolated data (c). The discretization of the radar image is $\Delta_{xy} = 0.05$ m and co-registration is considered.

If co-registration is not applied (second row of Figs. 9 and 10), the target appears slightly elongated in the along-track axis (y-axis) and the clutter level increases (compared to the previous results obtained applying co-registration). However, the number of measurements to process when both interpolation and co-registration are performed is around twice the number of measurements processed without interpolation (in the case of masked SAR) or without co-registration (in the case of PSM). This is because both forward and backward sweeps are interpolated into the same grid. Hence, as it will be shown later, if interpolation is performed, the processing time needed when applying co-registration is twice the time required when co-registration is not performed.

It is also of interest to analyze the effect of increasing the discretization step in the retrieved images. The results obtained with $\Delta_{xy} = \lambda_{min}/4 = 0.025$ m (and applying co-registration) are shown in the third row of Figs. 9 and 10. As can be observed, the images barely improve when compared to those obtained with $\Delta_{xy} = \lambda_{min}/2 = 0.05$ m. Thus it can be concluded that this discretization (i.e., $\Delta_{xy} = 0.05$ m) is dense enough to retrieve well-focused images.

Finally, it can be observed that the shape of the reconstructed targets in horizontal planes (i.e., $z = $ const.) is similar for all the considered processing methods (when co-registration is applied), indicating that the obtained cross-range resolution is comparable in all cases. In the range or z-axis, the proposed approach (comprising efficient interpolation and PSM) results in slightly narrower interfaces, as can be observed in Fig. 11 which corresponds to a vertical cut (at $x = 0.67$ m) of the first target. This, in turn, indicates that the range or depth resolution is slightly better for the proposed approach.

4.1.2. Quantitative radar image comparison

GPR imaging systems focus on maximizing the detection of buried targets and, to achieve this goal, one of the major challenges is related to effectively dealing with the clutter. Therefore, the Peak Signal to Clutter Ratio (PSCR), a metric to quantify the reflectivity level of each target with respect to the surrounding clutter, has been selected to assess the quality of the obtained images. The PSCR, which has been

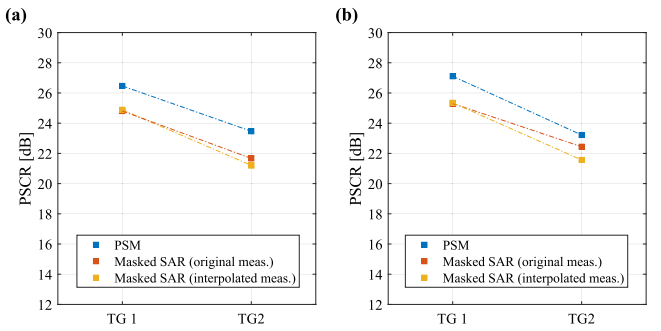

Fig. 12. Comparison of the PSCR for the first target (TG 1) and the second target (TG 2) when considering the different processing algorithms and applying co-registration. The discretization of the radar image is $\Delta_{xy} = 0.05$ m in (a), and $\Delta_{xy} = 0.025$ m in (b).

Fig. 13. Scenario of the validation tests with buried explosive targets.

computed for each target, is given by:

$$\text{PSCR [dB]} = 10\log_{10}\left(\frac{\max_{x,y\in A_t}|\rho(x,y,z_t)|^2}{\frac{1}{N_c}\sum_{x,y\in A_c}|\rho(x,y,z_t)|^2}\right), \tag{8}$$

where $\rho(x,y,z_t)$ is the radar image at the horizontal plane where the target is located (i.e., $z = z_t$), A_t and A_c correspond to the target and clutter regions, and N_c denotes the number of pixels within A_t. When computing the PSCR, the clutter region is limited to an area of 1 m×1 m centered at the target position (as the goal is to distinguish each target from its surroundings).

The PSCRs obtained for the two targets are shown in Fig. 12 considering the different processing algorithms and two discretization steps ($\Delta_{xy} = 0.05$ m in Fig. 12(a) and $\Delta_{xy} = 0.025$ m in Fig. 12(b)). The PSCRs corresponding to PSM processing are higher than those obtained with masked SAR, in agreement with the conclusions extracted from visually inspecting the radar images. Comparing the PSCRs for the two discretization steps, it can be concluded that the denser discretization usually provides a small improvement in the PSCR. However, this improvement does not justify the increase in the processing time. Therefore, the discretization step of $\Delta_{xy} = 0.05$ m has been selected for the experiments with buried explosive targets shown in Section 4.2.

4.1.3. Comparison of the processing times

The processing times are compared in Table 2 for the different processing algorithms and parameters (i.e., whether interpolation and/or co-registration are applied, and the value of Δ_{xy}). In case interpolation is performed, the interpolated positions are separated the same interval as the value of Δ_{xy}. The interpolation and processing methods have been executed on a laptop equipped with i7-8750H CPU and 32 GB of RAM.

Fig. 14. Targets in the validation tests after being unburied.

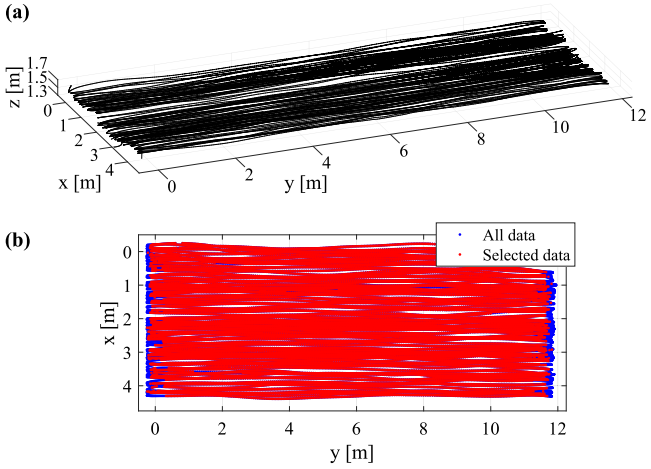

Fig. 15. Flight path (a) and measurement positions (b) in the validations tests with buried explosive targets (all positions in blue, and selected ones to be processed in red). (For interpretation of the references to color in this figure legend, the reader is referred to the web version of this article.)

Table 2
Comparison of the processing time required for the different processing algorithms in the initial tests. Number of selected measurement positions: 3741 (without interpolation), 3321 (interpolation with $\Delta_{xy} = 0.05$ m) and 13 041 (interpolation with $\Delta_{xy} = 0.025$ m).

Method	Interp.?	Δ_{xy} [m]	Coreg.?	Interp. [s]	Processing [s]	Total [s]
PSM	Yes	0.05	No	0.13	0.96	1.09
	Yes	0.05	Yes	0.24	1.94	2.18
	Yes	0.025	No	0.39	3.32	3.71
	Yes	0.025	Yes	0.66	6.60	7.26
Masked SAR	No	0.05	No	–	1973.43	1973.43
	No	0.05	Yes	–	1886.02	1886.02
	Yes	0.05	No	0.13	1787.80	1787.93
	Yes	0.05	Yes	0.24	3793.80	3794.04
	No	0.025	No	–	7982.18	7982.18
	No	0.025	Yes	–	7880.98	7880.98
	Yes	0.025	No	0.39	29 628.32	29 628.71
	Yes	0.025	Yes	0.66	64 160.38	64 161.04

When $\Delta_{xy} = 0.05$ m and co-registration are applied (first row of Figs. 9 and 10), the processing time required by PSM is only 2.18 s, whereas for masked SAR it increases up to 1886.02 s when the original measurements are used and to 3794.04 s when using the interpolated data. This shows a drastic reduction in the processing time when PSM is used. In particular, using PSM to retrieve the 3D GPR-SAR image is 865 times faster than considering masked SAR with the original measurements, and 1740 times faster than using masked SAR with the interpolated data. As observed in Table 2, the significant improvement in the processing time is even greater when considering $\Delta_{xy} = 0.025$ m.

4.2. Validation with buried explosive targets

The second validation scenario corresponds to a 4.5 m×12 m section of a dirt road, where different explosive targets have been buried.

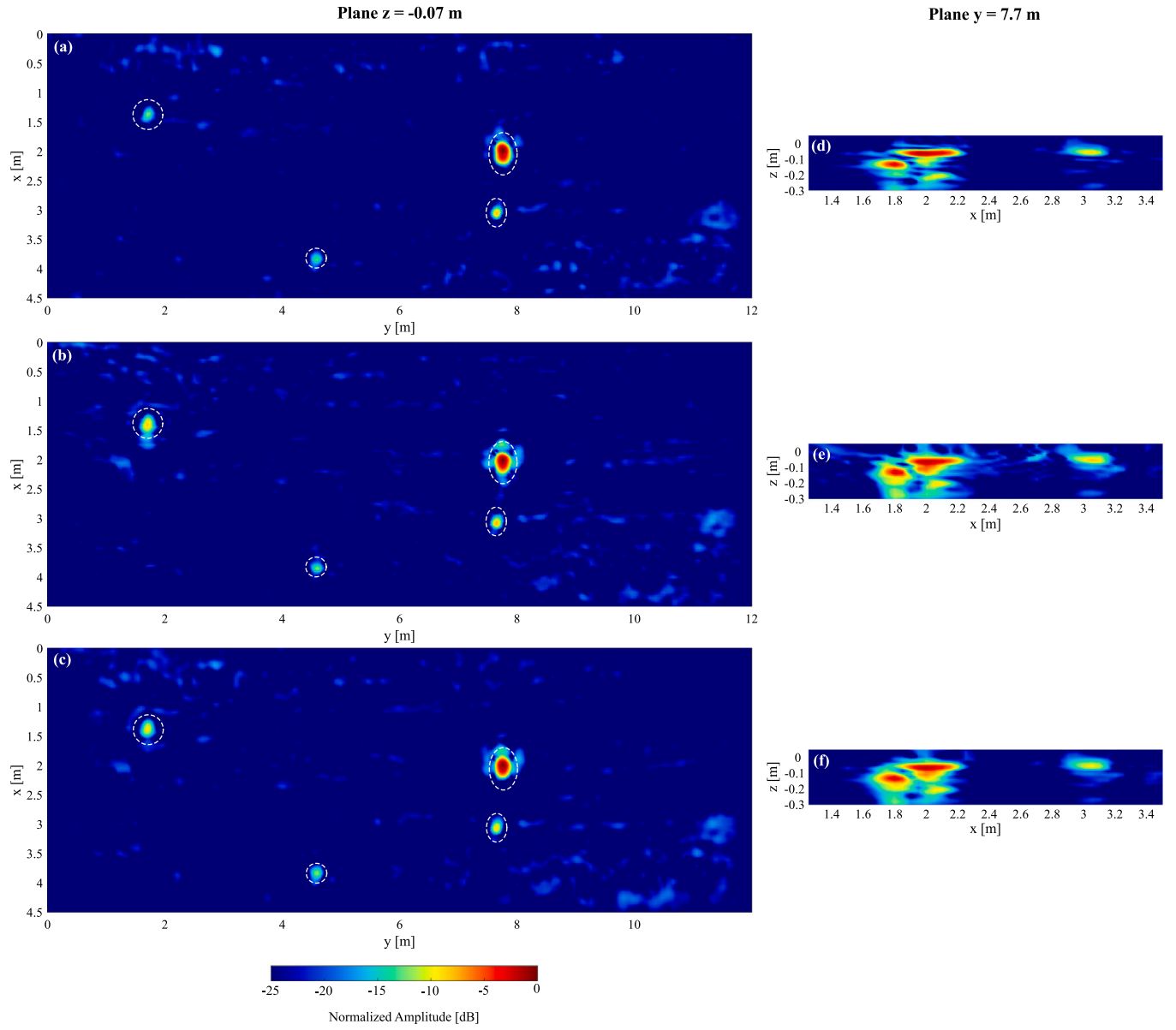

Fig. 16. Comparison of a horizontal cut (at $z = -0.07$ m, first column) and part of a vertical cut (at $y = 7.70$ m, second column) of the radar images retrieved when considering the different processing algorithms: PSM (a, d), masked SAR with the original data (b, e) and masked SAR with the interpolated data (c, f). The areas close to the targets in the horizontal cut are indicated with a white dashed circle.

Table 3
Targets buried in the second validation scenario.

Target	Size	Depth	Composition
AT landmine	35 cm × 35 cm × 10 cm	10 cm	Plastic
Battery	15 cm × 12 cm × 7.5 cm	13 cm	Metallic
Jug	40 cm × 28 cm × 20 cm	6 cm	Plastic (filled with fertilizer)
Pressure plate	29 cm × 7 cm × 4 cm	5 cm	Wood
Submunitions	Spheres of ⌀8.5 cm	5 cm	Metallic

In particular, these targets are: a low metal content anti-tank (AT) landmine, an IED composed of a jug (filled with fertilizer to simulate an explosive material) and a battery next to it, a wooden pressure plate (PP) and two small submunitions. A picture of the scenario during the inspection in shown in Fig. 13 and a picture of the scenario after the targets were unburied is shown in Fig. 14. In addition, the main characteristics of the buried targets are summarized in Table 3.

Analogously to the previous tests, the flight path is depicted in Fig. 15. The total number of selected positions to be processed is 25 625 (i.e., 51 250 measurements). When interpolation is performed (into a regular grid of 4.5 m × 12 m sampled at a $\lambda_{min}/2 = 0.05$ m interval), the resulting number of interpolated positions is 21 931.

The 3D GPR-SAR images are computed in a volume of 4.5 m × 12 m × 0.4 m discretized in voxels of $\Delta_{xy} \times \Delta_{xy} \times 0.01$ m. According to the conclusions extracted in the previous section, Δ_{xy} is set to 0.05 m, which results in $91 \times 241 \times 41 = 899171$ voxels.

4.2.1. Qualitative radar image comparison

The retrieved 3D GPR-SAR images are first compared qualitatively. For this purpose, the horizontal cut at $z = -0.07$ m (where reflections from most targets can be distinguished) and an across-track section at $y = 7.7$ m (corresponding to the IED composed by the jug and a battery, together with the pressure plate) are depicted in Fig. 16. Results obtained when considering PSM are depicted in Fig. 16(a, d), for masked SAR with the original data in Fig. 16(b, e) and for masked SAR with the interpolated data in Fig. 16(c, f). Co-registration has been applied in all cases since it provides better focused images. In the horizontal cuts,

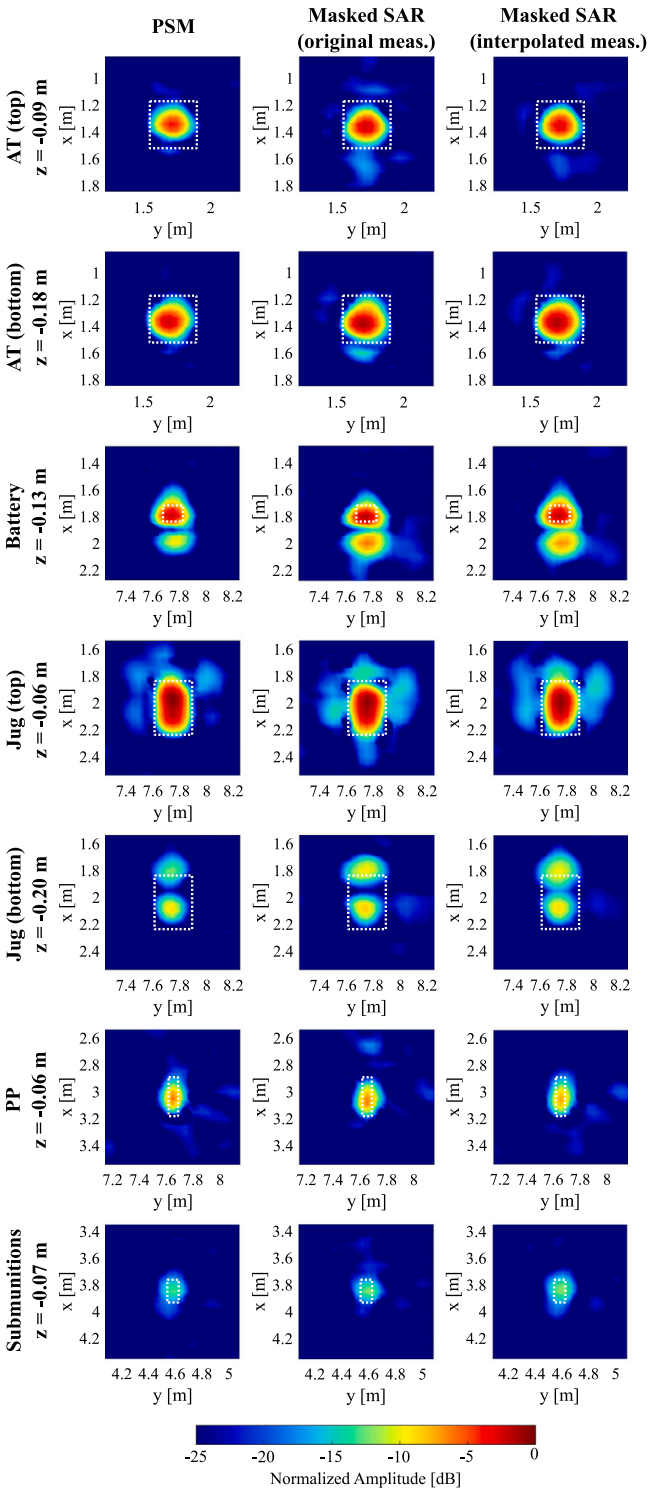

Fig. 17. Comparison of the radar images retrieved for each target considering the different processing algorithms (PSM in the first column, masked SAR with the original data in the second column and masked SAR with the interpolated data in the third column). The position of the targets is indicated with a white dashed line.

reflections proceeding from all targets (except the battery, which is buried significantly deeper) can be clearly distinguished. In the selected across-track section, both the top and bottom faces of the jug, the battery and the pressure plate are detected.

In agreement with the conclusions obtained in the initial tests (Section 4.1), the results obtained with masked SAR exhibit slightly

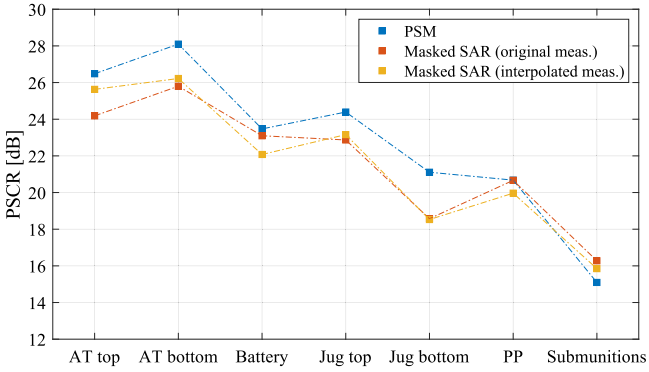

Fig. 18. Comparison of the PSCR for the targets shown in Fig. 17 when considering the different processing algorithms and applying co-registration.

Table 4
Comparison of the processing time required for the different processing algorithms in the tests with buried explosive targets. Number of selected measurement positions: 25 625 (without interpolation) and 21 931 (interpolation with $\Delta_{xy} = 0.05$ m).

Method	Interp.?	Coreg.?	Interp. [s]	Processing [s]	Total [s]
PSM	Yes	No	0.89	7.58	8.47
	Yes	Yes	2.14	14.47	16.61
Masked SAR	No	No	–	88 917.37	88 917.37
	No	Yes	–	88 852.03	88 852.03
	Yes	No	0.89	76 735.69	76 736.58
	Yes	Yes	2.14	152 456.55	152 458.69

higher clutter levels. This can be especially noticed in the vicinity of the jug, and when inspecting the across-track section.

In order to further compare the results obtained with the different processing strategies, horizontal sections of the radar image (at the depth at which each target is detected) are shown in Fig. 17. Comparing the results of masked SAR, it can be concluded that the images obtained with the interpolated measurements (third column of Fig. 17) usually exhibit slightly smaller clutter levels than those retrieved from the original data (second column of Fig. 17). In particular, this improvement is more evident for the top and bottom of the AT landmine and for the top of the jug. When PSM is considered (first column of Fig. 17), the clutter levels are further reduced, especially in the case of the battery and the top and bottom of the jug.

4.2.2. Quantitative radar image comparison

To quantitatively assess the imaging performance, the PSCR has been computed for all the targets depicted in Fig. 17 when considering the different processing strategies.

The obtained PSCR values, shown in Fig. 18, show that PSM provides the best PSCR for the majority of the targets, in agreement with the conclusions extracted from visual inspection of the retrieved radar images. The only exception is the submunitions, where PSM provides a slightly lower PSCR.

4.2.3. Comparison of the processing times

Finally, Table 4 provides a comparison of the processing times for the different processing strategies. For the results shown in Figs. 16 and 17 (i.e., applying co-registration), the processing time of PSM is only 16.61 s. This is a drastic improvement compared to the time required by masked SAR (88 852.03 s when using the original measurements and 152 458.69 s for the interpolated ones). In particular, the improvement reaches a factor of 5349 and 9179 depending on whether interpolation is performed.

These results show that using the proposed interpolation approach and PSM does not only result in a drastic reduction of the processing time, but also in an improvement of the signal to clutter ratio in the retrieved radar images.

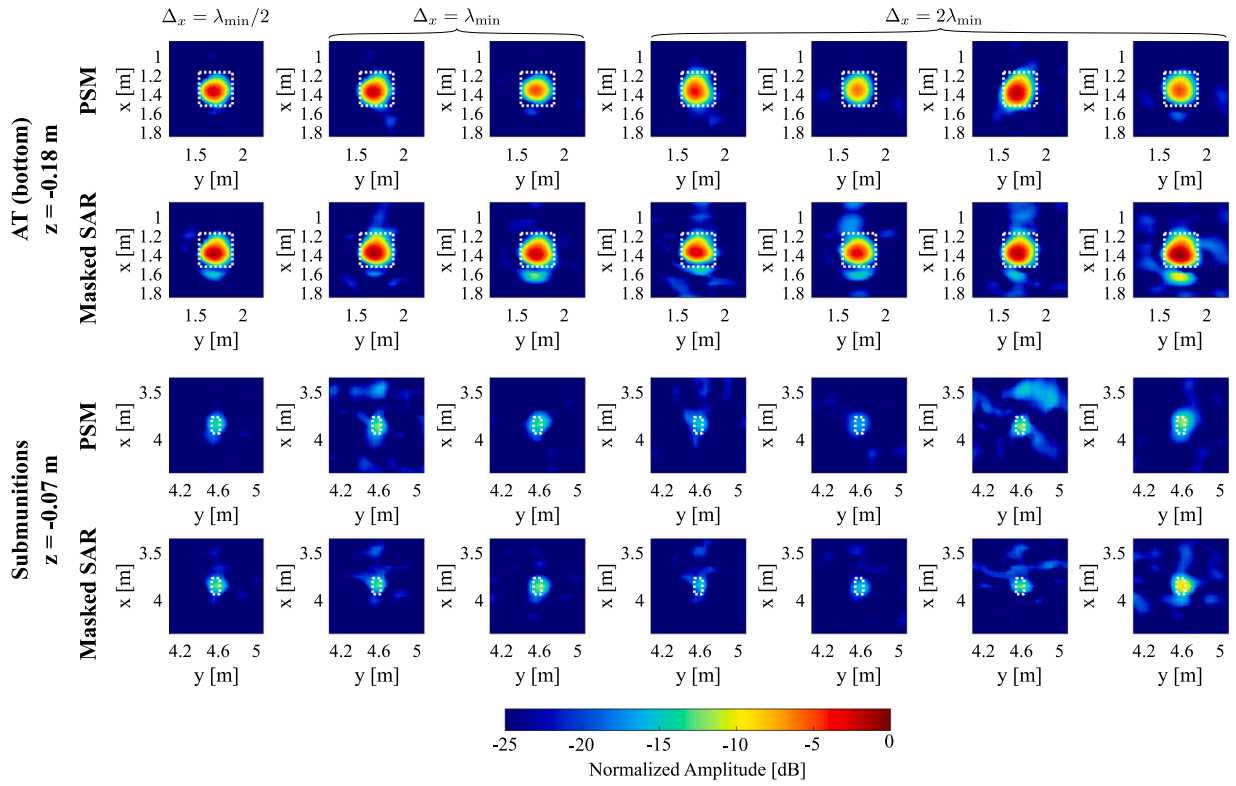

Fig. 19. Comparison of the radar images retrieved for the bottom of the AT landmine considering PSM (first row) and masked SAR (second row); and for the submunitions considering PSM (third row) and masked SAR (fourth row). Each column corresponds to a different set of along-track sweeps: all sweeps, i.e., $\Delta_x = \lambda_{\min}/2$ (1st column), one in two sweeps, i.e., $\Delta_x = \lambda_{\min}$ (2nd and 3rd columns), and one in four sweeps, i.e., $\Delta_x = 2\lambda_{\min}$ (4th to 7th columns).

4.2.4. Assessment of sparse flight paths

As previously explained, the along-track sweeps are separated an across-track distance of $\Delta_x = \lambda_{\min}/2 = 0.05\,\text{m}$, in agreement with the spatial sampling criterion considered in microwave imaging systems (Sheen et al., 2001). In general, increasing the sampling step beyond $\lambda_{\min}/2$ is expected to result in a deterioration of the imaging performance. Nevertheless, it is of interest to study the impact of increasing the across-track distance on the image quality. For this purpose, half of the sweeps of the original flight path in this second scenario have been selected to synthesize two sparse flight paths with $\Delta_x = \lambda_{\min} = 10\,\text{cm}$ (i.e., every other along-track sweep is selected starting from (i) the first sweep, whose results are shown in the 2nd column of Fig. 19, and from (ii) the second sweep, whose results are depicted in the 3rd column of Fig. 19). Similarly, one in four sweeps have been selected to generate four flight paths with $\Delta_x = 2\lambda_{\min} = 20\,\text{cm}$ (i.e., one in four along-track sweeps is selected starting from (i) the first sweep, 4th column of Fig. 19; (ii) the second sweep, 5th column of Fig. 19; (iii) the third sweep, 6th column of Fig. 19; and (iv) the fourth sweep, 7th column of Fig. 19). All these sparser flight paths have been processed with the proposed approach (efficient interpolation and PSM) and with a conventional backprojection algorithm (masked SAR, without interpolation). To illustrate the performance of the algorithms on the sparser flights, Fig. 19 shows the comparison of the radar images for one of the big targets (the bottom of the AT landmine) and the smallest one (the submunitions), when considering PSM and masked SAR for different across-track distances Δ_x.

As the radar subsystem comprises two receiving channels working simultaneously, the across-track distance can be relaxed to $\Delta_x = \lambda_{\min}$ (i.e., 10 cm) without significantly affecting the detection capabilities. In particular, all the buried targets are clearly detected although, in general, the clutter level is higher as less information is exploited. This can be observed in the 2nd and 3rd columns of Fig. 19 for the bottom of the AT landmine and the submunitions.

If the across-track distance is further increased, the deterioration in the imaging quality becomes more noticeable. In particular, if $\Delta_x = 2\lambda_{\min}$ (i.e., 20 cm), the medium and big size buried targets can be still detected, although, depending on the selected set of along-track sweeps, the reconstructed sizes and/or shapes of the targets may differ more from the actual ones, and the clutter levels are higher. However, for small targets (i.e., the submunitions), this sparse sampling step in the across-track direction can compromise their detection, as can be observed in the results shown in the 4th and 5th columns of Fig. 19.

These results also demonstrate that the proposed approach (comprising an efficient interpolation and PSM) can work with sparser schemes, achieving similar imaging results as conventional backprojection algorithm but requiring significantly less computational time.

5. Conclusions

In this work, a method to enable the adoption of migration-based algorithms, such as PSM, for UAV-mounted GPR imaging systems has been developed. The ultimate goal is to reduce the time required to retrieve the 3D GPR-SAR images, achieving close to real-time operation. Current prototypes mostly rely on backprojection algorithms, as they are able to deal with measurements gathered at arbitrary positions. However, these algorithms suffer from a high computational complexity. Hence, the proposed methodology, which efficiently combines a height shift operation (to project the GPR measurements onto a single plane) with a 2D interpolation (based on Delaunay triangulation), is key to overcoming this major bottleneck.

First, the accuracy of the proposed height shift operation has been analyzed, showing that the error induced by this step is significantly smaller than the minimum working wavelength. Furthermore, the improvement in the time required to perform the 2D interpolation (instead of a full 3D interpolation) has been also studied, showing significant time savings.

Then, the proposed approach (relying on height shift, efficient 2D interpolation, and PSM processing) has been validated with measurements gathered in two different scenarios. Its performance has been compared with that achieved using a conventional backprojection algorithm (called masked SAR) in terms of processing time and imaging capabilities. It has been demonstrated that the method developed in this work enables a drastic improvement in the reconstruction time. In addition, the resulting 3D GPR-SAR images have been compared with those obtained with masked SAR (both qualitative and quantitatively), showing that the proposed approach provides images with slightly less clutter.

As an example, in the case of the second scenario (with buried explosive threats), the time required when applying the conventional masked SAR processing is over 88 800 s for an image reconstructed in a volume larger than 21 m^3 (in particular, 41 horizontal slices of 54 m^2). However, in the same scenario, the proposed methodology reduces the processing time to less than 17 s when applying co-registration and to less than 9 s when co-registration is not performed, i.e., 5349 and 10 498 times faster respectively.

Funding

This work has been funded by the Ministry of Defense - Government of Spain and by the University of Oviedo, Spain under Contract 2019/SP03390102/00000204/CN-19-002 (“SAFEDRONE”); by Project PID2021-122697OB-I00 funded by MCIN/AEI/10.13039/501100011033/FEDER, UE; by the UKRI Postdoctoral Fellowship Guarantee for MSCA PF, UK under Project EP/X022943/1 and Project EP/X022951/1; and by Gobierno del Principado de Asturias/FEDER, Spain under grant AYUD/2021/51706. Data supporting this study cannot be made available due to legal/security concerns.

Declaration of competing interest

The authors declare that they have no known competing financial interests or personal relationships that could have appeared to influence the work reported in this paper.

Acknowledgments

The authors would like to thank the personnel of the Counter Improvised Explosive Devices Center of Excellence (C-IED CoE) (C-IED CoE, 2022) and the Ministry of Defense of Spain for their counseling and support on the topic of landmine and IED detection.

References

Alvarez, Y., Garcia, M., Arboleya, A., Gonzalez, B., Vaqueiro, Y.R., Las-Heras, F., Pino, A.G., 2017. SAR-based technique for soil permittivity estimation. Int. J. Remote Sens. 38, 5168–5186.

Alvarez Lopez, Y., Garcia-Fernandez, M., Alvarez-Narciandi, G., Las-Heras Andres, F., 2022. Unmanned aerial vehicle-based ground-penetrating radar systems: A review. IEEE Geosci. Remote Sens. Mag. 2–22. http://dx.doi.org/10.1109/MGRS.2022.3160664.

Amidror, I., 2002. Scattered data interpolation methods for electronic imaging systems: a survey. J. Electron. Imaging 11 (2), 157–176.

Burr, R., Schartel, M., Grathwohl, A., Mayer, W., Walter, T., Waldschmidt, C., 2021. UAV-borne FMCW InSAR for focusing buried objects. IEEE Geosci. Remote Sens. Lett. 1–5. http://dx.doi.org/10.1109/LGRS.2021.3094165.

2022. Counter improvised explosive devices center of excellence (C-IED CoE). URL https://www.ciedcoe.org/.

Catapano, I., Gennarelli, G., Ludeno, G., Noviello, C., Esposito, G., Soldovieri, F., 2022. Contactless ground penetrating radar imaging: State of the art, challenges, and microwave tomography-based data processing. IEEE Geosci. Remote Sens. Mag. 10 (1), 251–273.

Fallahpour, M., Case, J.T., Ghasr, M.T., Zoughi, R., 2014. Piecewise and Wiener filter-based SAR techniques for monostatic microwave imaging of layered structures. IEEE Trans. Antennas and Propagation 62 (1), 282–294.

Garcia-Fernandez, M., Alvarez-Lopez, Y., Arboleya-Arboleya, A., Gonzalez-Valdes, B., Rodriguez-Vaqueiro, Y., Las-Heras, F., Pino-Garcia, A., 2018. Synthetic aperture radar imaging system for landmine detection using a ground penetrating radar on board a unmanned aerial vehicle. IEEE Access 6, 45100–45112.

Garcia-Fernandez, M., Alvarez-Lopez, Y., Las-Heras, F., 2019. Autonomous airborne 3D SAR imaging system for subsurface sensing: UWB-GPR on board a UAV for landmine and IED detection. Remote Sens. 11 (20).

Garcia-Fernandez, M., Alvarez-Lopez, Y., Las-Heras, F., 2020. Airborne multi-channel ground penetrating radar for improvised explosive devices and landmine detection. IEEE Access 8, 165927–165943.

Garcia-Fernandez, M., Alvarez-Narciandi, G., Alvarez-Lopez, Y., Las-Heras, F., 2022. Comparison of subsampling strategies for UAV-mounted subsurface radar imaging systems. In: 2022 IEEE AP-S Symposium on Antennas and Propagation.

García-Fernández, M., Álvarez-Narciandi, G., Álvarez López, Y., Las-Heras Andrés, F., 2021. Analysis and validation of a hybrid forward-looking down-looking ground penetrating radar architecture. Remote Sens. 13 (6), http://dx.doi.org/10.3390/rs13061206.

García-Fernández, M., Álvarez-Narciandi, G., Álvarez López, Y., Las-Heras Andrés, F., 2022. Improvements in GPR-SAR imaging focusing and detection capabilities of UAV-mounted GPR systems. ISPRS J. Photogramm. Remote Sens. 189, 128–142.

García-Fernández, M., Álvarez-Narciandi, G., Álvarez López, Y., Las-Heras Andrés, F., 2023. Array-based ground penetrating synthetic aperture radar on board an unmanned aerial vehicle for enhanced buried threats detection. IEEE Trans. Geosci. Remote Sens. 61, 5104218.

García Fernández, M., Álvarez Narciandi, G., Arboleya, A., Vázquez Antuña, C., Andrés, F.L.-H., Álvarez López, Y., 2021. Development of an airborne-based GPR system for landmine and IED detection: Antenna analysis and intercomparison. IEEE Access 9, 127382–127396. http://dx.doi.org/10.1109/ACCESS.2021.3112058.

Gennarelli, G., Noviello, C., Ludeno, G., Esposito, G., Soldovieri, F., Catapano, I., 2023. Three-dimensional ray-based tomographic approach for contactless GPR imaging. IEEE Trans. Geosci. Remote Sens. 61, 200614.

González-Díaz, M., García-Fernández, M., Álvarez-López, Y., Las-Heras, F., 2020. Improvement of GPR SAR-based techniques for accurate detection and imaging of buried objects. IEEE Trans. Instrum. Meas. 69 (6), 3126–3138.

Grathwohl, A., Arendt, B., Timo, G., Waldschmidt, C., 2023. Detection of objects below uneven surfaces with a UAV-based GPSAR. IEEE Trans. Geosci. Remote Sens. 61, 5207913.

Grathwohl, A., Hinz, P., Burr, R., Steiner, M., Waldschmidt, C., 2021. Experimental study on the detection of avalanche victims using an airborne ground penetrating synthetic aperture radar. In: 2021 IEEE Radar Conference. RadarConf21, pp. 1–6. http://dx.doi.org/10.1109/RadarConf2147009.2021.9455286.

Jenssen, R.O.R., Eckerstorfer, M., Jacobsen, S., 2020. Drone-mounted ultrawideband radar for retrieval of snowpack properties. IEEE Trans. Instrum. Meas. 69 (1), 221–230. http://dx.doi.org/10.1109/TIM.2019.2893043.

Johansson, E.M., Mast, J.E., 1994. Three-dimensional ground-penetrating radar imaging using synthetic aperture time-domain focusing. In: Udpa, S.S., Han, H.C. (Eds.), In: Advanced Microwave and Millimeter-Wave Detectors, vol. 2275, SPIE, International Society for Optics and Photonics, pp. 205–214.

Narciandi, G.Á., Laviada, J., Las-Heras, F., 2021. Towards turning smartphones into mmwave scanners. IEEE Access 9, 45147–45154.

Noviello, C., Esposito, G., Catapano, I., Soldovieri, F., 2021. Multilines imaging approach for mini-UAV radar imaging system. IEEE Geosci. Remote Sens. Lett. 1, 1–5.

Noviello, C., Gennarelli, G., Esposito, G., Ludeno, G., Fasano, G., Capozzoli, L., Soldovieri, F., Catapano, I., 2022. An overview on down-looking UAV-based GPR systems. Remote Sens. 14 (14).

Regmi, H., Saadat, M.S., Sur, S., Nelakuditi, S., 2021. SquiggleMilli: approximating SAR imaging on mobile millimeter-wave devices. In: Proceedings of the ACM on Interactive, Mobile, Wearable and Ubiquitous Technologies. 5, (3).

Sheen, D., McMakin, D., Hall, T., 2001. Three-dimensional millimeter-wave imaging for concealed weapon detection. IEEE Trans. Microw. Theory Tech. 49 (9), 1581–1592. http://dx.doi.org/10.1109/22.942570.

Sipos, D., Gleich, D., 2020. A lightweigth and low-power UAV-Borne ground penetrating radar design for landmine detection. Sensors 20, 2234.

Stolt, R.H., 1978. Migration by Fourier transform. Geophysics 43 (1), 23–48.

Vasileiou, C., Smith, J., Thiagarajan, S., Nigh, M., Makris, Y., Torlak, M., 2022. Efficient CNN-based super resolution algorithms for mm-wave mobile radar imaging. In: 2022 IEEE International Conference on Image Processing. ICIP, pp. 3803–3807.

Wu, K., Rodriguez, G.A., Zajc, M., Jacquemin, E., Clément, M., De Coster, A., Lambot, S., 2019. A new drone-borne GPR for soil moisture mapping. Remote Sens. Environ. 235, 111456. http://dx.doi.org/10.1016/j.rse.2019.111456.